nature portfolio

https://doi.org/10.1038/s41586-022-05130-0

Supplementary information

Tracking single adatoms in liquid in a transmission electron microscope

In the format provided by the authors and unedited

Guide to the Supplementary information supplied for "Tracking single adatoms in liquid in a Transmission Electron Microscope"

Supplementary Information contains:

Double liquid cell fabrication details and low magnification images, electron diffraction through single cell, EEL mapping of oxygen (water) content in cell, EDXS mapping of Pt clusters, details of additional videos, consideration of radiation damage, further details of image processing, additional images of Pt adatoms at different lattice sites, full details of atomic position and trajectory analysis as well as the statistics of Pt adatom motion, details of DFT calculations.

Supplementary Videos:

Video 1: Liquid cell magnification series

Raw HAADF STEM image series of Pt filled MoS_2 double graphene liquid cell with increasing magnification. Pt nanocrystals and individual Pt atoms are seen at the highest magnification.

Videos 2-3: Liquid cell focal series

Raw HAADF STEM image series of Pt filled MoS_2 double graphene liquid cell while changing focus in different regions of interest. Pt nanocrystals and individual Pt atoms are seen to come into sharp focus at different focal depths corresponding to the positions of the different membranes (two graphene or MoS_2) in the liquid cell.

Video 4: Unprocessed Liquid Cell Pt motion on MoS_2 video

Raw HAADF STEM image series showing motion of Pt adatoms on monolayer MoS_2 inside a double graphene liquid cell. The probe current was 160 pA, and the pixel dwell time was 6µs, so each 512 x 512 image took 1.57s to record. Successive images were started every 2s. The pixel step size was 0.34 Å, and electron flux per frame was 5.2 x 10^6 e.nm^{-2}, and the averaged electron fluence during the video was 2.6 x 10^6 e.s^{-1}.nm^{-2}. Total video running time was 176s.

Video 5: Unprocessed Vacuum Pt motion on MoS_2 video

Raw HAADF STEM image series showing motion of Pt adatoms on monolayer MoS_2 in vacuum. The probe current was 160 pA, and the pixel dwell time was 4µs, so each 1024 x 1024 image took 4.19s to record. Successive images were started every 5s. The pixel step size was 0.24 Å, so the electron flux per frame was therefore 6.9 x 10^6 e.nm^{-2}, and the averaged electron fluence during the video was 1.4 x 10^6 e.s^{-1}.nm^{-2}. Total video running time was 327s.

Video 6: Processed Liquid Cell Pt motion and extracted Pt trajectories

The left panel shows the HAADF STEM image series shown in supplementary video 4, after drift, shear and rotation correction. The right panel shows extracted Pt adatom positions (red spheres) relative to the measured Mo site locations (purple spheres) and inferred S site locations. Pt atom trajectories are shown with a colour scale from blue (start) to green, yellow, orange then red.

Video 7: Processed Vacuum Pt motion and extracted Pt trajectories

The left panel shows the ADF STEM image series shown in supplementary video 5, after drift, shear and rotation correction. The right panel shows extracted Pt adatom positions (red spheres) relative to the measured Mo site locations (purple spheres) and inferred S site locations. Pt atom trajectories are shown with a colour scale from blue (start) to green, yellow, orange then red.

Video 8: Single Pt adatom motion in liquid cell

Left panel contains drift corrected ADF STEM image series showing motion of a single Pt adatom on MoS_2 lattice in water, as shown in figure 4a. Middle panel shows 'enhanced' image after template matching and reconstruction process. Right panel shows inferred atomic positions and the path traced by the Pt adatom. Pt atom trajectory is shown with a colour scale from blue (start) to green, yellow, orange then red.

Supplementary Information for: “Tracking single adatoms in liquid in a Transmission Electron Microscope”

Nick Clark[1,3], Daniel J. Kelly[1,3], Mingwei Zhou[2,3], Yi-Chao Zou[1,3,4], Chang Woo Myung[5], David G. Hopkinson[1,3], Christoph Schran[5], Angelos Michaelides[5], Roman Gorbachev[2,3]* and Sarah J. Haigh[1,3]^

[1]Department of Materials, University of Manchester, Oxford Road, Manchester M13 9PL, United Kingdom. [2]Department of Physics and Astronomy, University of Manchester, Oxford Road, Manchester M13 9PL, United Kingdom. [3]National Graphene Institute, University of Manchester, Oxford Road, Manchester M13 9PL, United Kingdom. [4]School of Materials Science and Engineering, Sun Yat-sen University, Guangzhou, 510275, PR China. [5]Yusuf Hamied Department of Chemistry, University of Cambridge, Lensfield Road, Cambridge CB2 1EW, United Kingdom.

**roman@manchester.ac.uk*

^sarah.haigh@manchester.ac.uk

Contents:

1. Liquid Cell Fabrication

The unique double graphene liquid cells in this work consist of a molybdenum disulphide (MoS_2) sheet encapsulated between two liquid cells, both with hexagonal boron nitride (hBN) spacer layers and graphene outer windows. They were fabricated by successively transferring flakes of mechanically exfoliated 2D materials to build the sandwich structure illustrated in figure 1 of the main text. This section provides further detail on the fabrication process. The stages of sample fabrication are illustrated schematically, with optical images showing the various stages of fabricating a cell, including the isolation of original flakes, in extended data figure 1.

To produce the patterned spacer layers hBN flakes were mechanically exfoliated onto an oxidised (90 nm) silicon (Si) wafer. Suitable flakes were optically selected for their size (20 - 100 μm laterally), good flatness and approximate thickness (determined based on colour[50]). Holes were then drilled through the selected hBN flakes by using electron beam lithography to define a poly(methyl methacrylate) PMMA etch mask, followed by reactive ion etching (using fluoroform (CHF_3) and oxygen (O_2)) to transfer the pattern to the hBN. Hole diameters of 100 - 600 nm were used as these have been found to allow a large specimen field of view with optimal filling of the liquid cells: larger diameters can result in incomplete ring filling as the graphene windows conform to the structure underneath (see supplementary information in ref. [17]). A brief oxygen etch is then used to functionalise the interior walls of the wells to make them more hydrophilic, whilst the upper surface is still protected by the PMMA mask. The mask was removed using organic solvent washing and subsequent annealing in a reducing atmosphere (5% hydrogen (H_2) in argon (Ar)). Atomic force microscopy (AFM) was then used to measure the hBN flake thickness and verify that no PMMA residue remained on the surface.

Next the 'bottom' few-layer graphene (FLG) window flake was exfoliated onto an oxidised silicon substrate. The suitable crystal was selected for its thickness (3 - 5 layer), relatively large lateral size (20 - 100 μm), and its being free of any visible defects/ bubbles/ tears using optical microscopy[51]. The bottom hBN spacer was then transferred onto the bottom FLG window by coating it in a PMMA layer and dissolving the silicon oxide substrate in weak potassium hydroxide (KOH) [52], before rinsing and drying, and placing onto the FLG flake using a micromanipulator[53]. Organic solvents and subsequent annealing were used to remove the transfer residue, for example washing in acetone and propan-2-ol before annealing for 30 minutes at 250 °C.

For the central membrane layer, the MoS_2 monolayer was exfoliated onto another oxidised Si wafer and either transferred as described above for the bottom hBN spacer or picked up directly using a polymer film[54]. The MoS_2 was then used to encapsulate a bottom 'liquid A' sample inside the bottom spacer layer by using a pipette to drop-cast the liquid sample between the flakes immediately before they were brought into contact, as shown in extended data figure 1a. Here liquid A is a 2:1 ratio of water: isopropanol. The sample was allowed to dry slowly at room temperature for 8 hours to ensure pockets were fully sealed, before the polymer layer was removed. The stack now consists of an array of sealed liquid cells with graphene lower windows and MoS_2 upper window.

To complete the double liquid cell structure the few-layer graphene flake (3 - 5 layer) for the 'top' window was exfoliated directly onto a polymer transfer film, and directly transferred[64] on to the 'top' hBN spacer. KOH was then used to dissolve the SiO_2 substrate, and the same polymer transfer layer was used to place the top hBN spacer, with the top FLG window attached, over the lower filled cells. To fill the upper liquid cell a 10 mM chloroplatinic acid (H_2PtCl_6) (purchased from Sigma-Aldrich UK) solution (in 2:1 water: propan-2-ol) was pipetted between the two layers immediately before the two parts were brought into contact, as shown in extended data figure 1b. The whole stack was then left to dry slowly. Finally, the completed double liquid cell stack was transferred to a custom silicon nitride (SiN_x) support membrane *via* a third transfer (*via* polymer deposition and KOH etching of the silicon oxide substrate), and finally cleaned using organic solvents (extended data figure 1c).

The fabrication process for our DGLCs is multi-staged and relatively labour intensive but produces liquid cells that are exceptionally robust, allowing for prolonged imaging at atomic resolution at high electron fluxes of 2.8 x 10^6 e^- s^{-1} nm^{-2}. In addition, a sample typically contains many 10s of individual double liquid regions

with each cell being separately sealed. This means that even if one cell is perforated and dehydrates in the vacuum, neighbouring cells can continue to be imaged in their hydrated state and a large amount of experimental data can be obtained from each DGLC. Furthermore, we note that the processing steps are capable of scale up such that in the future hundreds of DGLC TEM grids could be prepared simultaneously, without increasing the fabrication time significantly. One of the most challenging fabrication steps is transfer of the specimen to the TEM grid and we have recently demonstrated that the success rate for this can be increased to almost 100% using a new design of adhesion enhanced TEM support grid[21]. A limitation of the current design is the requirement for aqueous solutions in order to prevent adverse interaction with the polymeric support membrane (PMMA) used when closing the cell. We anticipate that this could be overcome in the future with further development of the fabrication steps, thereby enabling the study of organoplatinum or other organometallic compounds in organic solvents.

2. Consideration of the effects of the electron beam

Both graphene and MoS_2 are well known to be susceptible to knock-on damage degradation at the 200 kV accelerating voltage used in this work[32,55-58]. Nonetheless, we find that damage to the graphene windows can be minimised by: using a few-layer, rather than monolayer, graphene crystals; employing short dwell times when imaging; and avoiding focussing on the graphene membranes themselves with the STEM probe. We find that these measures prevent catastrophic failure of the graphene membranes and the resulting loss of water from either the upper or lower cells even after extended imaging at 200 kV. However, it is not possible to avoid focussing on and damaging the MoS_2 membrane so liquid can leak between the two layers. This is the key reason for the double graphene liquid cell structure. Having the MoS_2 monolayer fully submerged between two liquid pockets means that, even the presence of pin holes, tears or cracking in the membrane does not cause cell failure and the MoS_2 remains surrounded by liquid. If liquid is lost from the cell this is clearly visible as it results in a reduction of the background intensity level, accompanied by an improvement in image contrast. The presence or absence of water has also been verified using electron energy loss spectroscopy (EELS) as demonstrated in extended data figure 3. Furthermore, in the event of a loss of liquid from a particular liquid pocket, neighbouring pockets remain intact for further imaging.

An accelerating voltage of 60 - 80 kV is generally preferred when high resolution imaging of MoS_2 in vacuum to reduce the effect of knock on damage[32,57,59]. However, significant S vacancies are produced at both 60 and 200 kV (see Table S1 for a summary of estimated S vacancy generation for different imaging conditions) and the stronger beam-sample interactions at low accelerating voltage will also increase the potential for radiolytic changes in the chemistry of the liquid layer[12,60]. Here we use mechanically exfoliated MoS_2 so the number of native S vacancies is low (approximately $4.6 \pm 1 \times 10^{12}$ cm^{-2}) [28,61] and electron beam generated vacancies are likely to be dominant. However, MoS_2 materials with much higher quantities of intrinsic S vacancies exist and are preferred for improved performance towards the hydrogen evolution reaction[29,62]. In practice, a key benefit of the higher accelerating voltage is likely to be the greater tolerance to specimen thickness, and hence liquid volume, compared to lower voltages. It is likely that the choice of accelerating voltage for double liquid cell experiments will depend on the precise experimental conditions, including signal to noise ratio, spatial resolution required, materials and solution chemistry.

Table S1: *Estimated number of single sulphur vacancies created per frame using imaging conditions in this work and those used by Li et al.[30] (indicated by *). Vacancy creation rate at 200 kV was estimated using a cross section of 140 barn from Komsa et al.[57]. Vacancy creation rate at 60kV was estimated using a cross section of 7 barn from Kretschmer et al.[58]. For our work all frames have same resolution and dwell time, except video #7 which used a 1024,1024 rather than a 512,512 scan area.*

Accelerating Voltage	**Beam Current** (pA)	**SVac created per frame**
200 kV	42	66
	81	130
	167	260
	167 (video #7)	690
60 kV	42	3.3
	81	6.3
	167	13
	167 (video #7)	35
	44 (min dwell T)*	5.7
	44 (max dwell T)*	23

The electron fluence and energy will also influence the local chemistry of the liquid sample. During electron irradiation of water, a variety of reaction products/ radical species are created, including molecular hydrogen (H_2), hydrogen peroxide (H_2O_2), hydroxyl radical ($HO^{\bullet}$), hydrogen and hydroxide ions (H^+ and OH^-), molecular oxygen (O_2), superoxide (O_2^-), oxygen ions (O^-) and others, in concentrations which are dependent on total dose, dose rate, and irradiation pattern[63]. In our system, formation of these radiolysis

products should be supressed by the addition of isopropanol[12,64], and the use of graphene windows[65], both of which scavenge the produced radicals. Studies demonstrating the scavenging effect have only been carried out in significantly larger liquid volumes than those tested here, and it is unclear whether the reduced dimensionality affects the scavenging behaviour by limiting diffusion, or what the effect of the MoS_2 surface could have. If we assume that all hydrogen and hydroxyl radicals are immediately scavenged, there are still possible formation pathways for other species such as molecular oxygen (O_2) and hydrogen peroxide (H_2O_2), which are likely to be present in our system in concentrations which depend on the electron fluence. Both O_2 and H_2O_2 can interact with a sulphur vacancy leading to the incorporation of an oxygen atom into the lattice[31,66], which becomes a less favourable adsorption site for Pt (see SI section 6). Molecular oxygen (O_2) can also bind on a sulphur vacancy[67,68], and can preferentially dissociate on the pristine MoS_2 surface leaving oxygen adatoms[66], which could then diffuse across the surface to fill S vacancy sites[69]. Any un-scavenged hydrogen and hydroxyl radicals can also be expected to interact with sulphur vacancies and the basal plane of transition metal dichalcogenides[70]. Any of these routes could affect the Pt adatom dynamics by changing the diffusion barrier or modifying the availability of favourable adsorption sites such as S vacancies.

Although native S vacancies in the materials could be passivated by the interaction with molecular oxygen in the air during specimen loading[31,66,67,69], this molecular oxygen passivation would be expected to desorb when the sample is loaded into the TEM vacuum[71,72]. The TEM's low gas pressure means that there is likely to be far less oxygen and chlorine species able to substitute into sulphur vacancies for the vacuum or dried samples, compared to the case where the liquid acts as a continuous source of oxygen and chlorine.

To fully understand the beam dependence would require unravelling the competing processes of vacancy and defect creation and migration in the substrate as well as the beam induced adatom motion. Some benefit would be obtained by being able to track the lighter S atoms, potentially achievable with the current optimized cell design combined with new efficient direct detector technologies to increase the signal to noise ratio still further.

3. Further details of Image Processing

Extended data figure 6 provides a summary of the image processing needed to recover both Pt adatom positions and the MoS_2 lattice for each frame in the HAADF STEM videos.

First, we describe the four patch based PCA (Principal Component Analysis) reconstruction algorithm[37,38] steps used to extract the MoS_2 lattice with reference to the numbers in extended data figure 6a-g. Note that before beginning this procedure the whole data set was drift corrected (pixel wise translation by whole pixels in x and y) using whole image cross correlation.

Select individual image patches (49 x 49 pixels) centred at bright peaks in the original image (a). Patches are multiplied by a central Gaussian such that the intensity is approximately radially symmetric. Example patches are shown in panel (b).

Perform PCA/decomposition on the stack of image patches to identify common components. First 8 components are shown in (c).

Select first n (here 18) 'principal' components and rebuild stack of patches using only these. Rebuilt patches are shown in panel (d).

Rebuilt patches are summed at their original locations and normalised to produce a reconstructed image.

In practice, the identification of bright peaks (atomic locations) was challenging in step 1, so the 4 steps were repeated using the first reconstructed image to help select lattice locations (from the original image) to generate a second.

The method described has the effect of removing any non-periodic/ repeating features due to contamination and noise and enables us to determine the positions of the Mo atomic lattice sites. A direct comparison of original, Gaussian filtered and patch reconstructed data for a small region of supplementary video 4 is shown in figure S1, along with intensity profiles to aid comparison. This clearly demonstrates the improvement in signal to noise ratio which is necessary for identification of the underlying MoS_2 substrate lattice. This method performed satisfactorily for each frame in each image sequence (with three different electron doses) using the same parameters.

Mo lattice sites in each frame (extended data figure 6j) were found using peak finding on the reconstructed image (panel g), and linked frame to frame using a nearest neighbour algorithm. The mean displacement of the Mo sites in each frame was used to perform a second pixelwise drift correction step on both the original video and the 'rebuilt' image.

It is clear from the reconstructed result in (extended data figure 6g) that the location of the Pt adatom positions is lost and hence these must be recovered by separate image processing steps. To achieve this the drift corrected raw video (panel a) was filtered in Fourier space, and thresholded to generate an 'adatoms' image (panel e) and an image which highlighted holes in the MoS_2 lattice (panel f). The 'holes' image was segmented to identify hole locations, where Mo lattice was not present, which could be used to remove identified Mo sites, shown in red in extended data figure 6j), from the template rebuilt image (panel g). Peak-finding was also performed on the adatoms image in extend data figure 6e to generate tentative Pt adatom sites (panel h). The relative offset between each adatom and its nearest neighbour Mo site was calculated and used to categorise adatoms as being positioned on Mo, S, or HC sites, as indicated in extended data figure 6i (red dots for 'none' or HC, purple for Mo, yellow for S). Examples of Pt adatoms identified at Mo, S and HC sites are shown in figure S2 and in figure 2 in the main text.

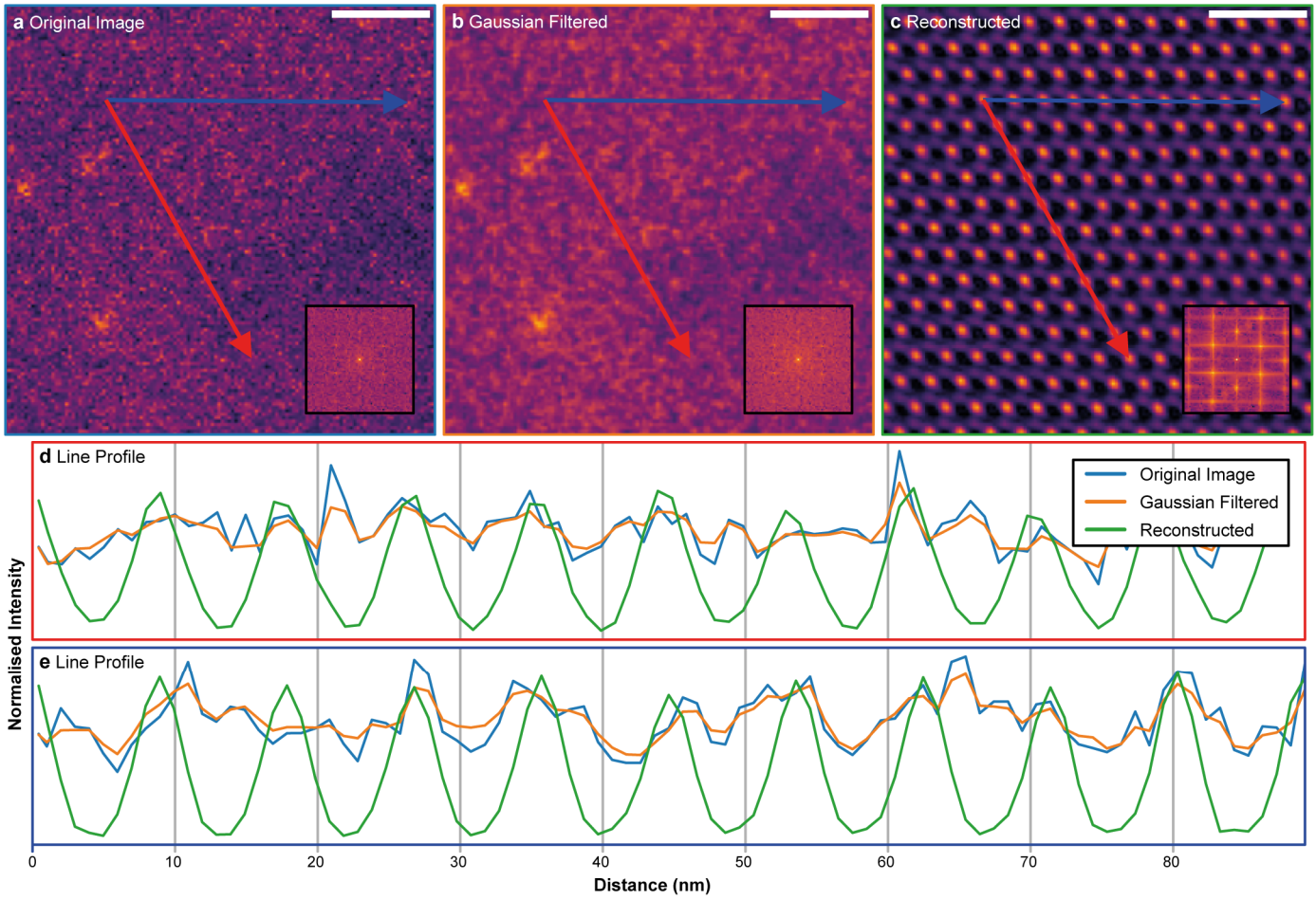

Figure S1: Result of template matching process. *Comparison of image regions from supplementary video 4 (liquid cell Pt adatom motion) showing (a) the raw HAADF STEM image, (b) image after Gaussian blur with a radius of 1.6 px, (c) reconstructed image after template matching. (d, e) Intensity profiles along the red and blue arrows demonstrating the improvement in SNR for the underlying Mo lattice sites. Scale bars are 2 nm.*

To study the motion of the Pt adatoms on the surface of the MoS_2 layer we have linked the identified peaks in the adatoms frame using a minimal nearest neighbour approach[39], where jump distances between adatoms in adjacent frames were minimised, to reconstruct atomic trajectories (extended data figure 6k). This is necessary because, unlike nanocluster analysis, single Pt atoms are indistinguishable from each other and there was no motion correlation from frame to frame. Adatom positions within <1.1 nm were considered as potentially belonging within the same trajectory, and a 3 frame 'memory' was used allowing linking of trajectories even where the adatom is not present for a few frames, as is possible for a serial acquisition technique such as STEM.

The assumption of nearest neighbour hopping has the possible effect of underestimating the calculated mean square displacement (MSD) at longer lag times, as when there is more than one particle within the search distance we cannot be sure we have linked the correct particles. To investigate this effect, we also calculated the MSDs using only those parts of identified trajectories where there was only a single atom within the local search distance (~ 1 nm radius). The result was almost identical to the complete data set suggesting the assumption is valid (although the experimental uncertainty was increased at longer lag times). These 'isolated' MSDs for 4 representative videos are shown in extended data figure 7d.

To enable analysis of adatom trajectories independent of the movement of the MoS_2 lattice, identified Mo site positions were then averaged over their lifetimes to generate 'stationary' positions for each Mo atom in the lattice. An additional drift correction step was performed by comparing the identified Mo site locations (extended data figure 6k) in each frame to their 'stationary' positions to calculate an affine transform (panel

m) which could be used to map the frame positions on to the average positions (taking into account shear, rotation, and scale as well as translation). The identified transform each frame was then applied to the Pt positions to generate adatom trajectories relative to the MoS_2 lattice (panel l). Selected example trajectories are shown in figure S3 as well as in figure 4b in the main text.

For further analysis (figures S6-8, extended data figures 7-8, and figures 3-4 in main text) we only considered those parts of trajectories outside manually chosen Pt clumps, as in that shown by blue circle in figure S5, where the Pt tracking algorithm was ineffective.

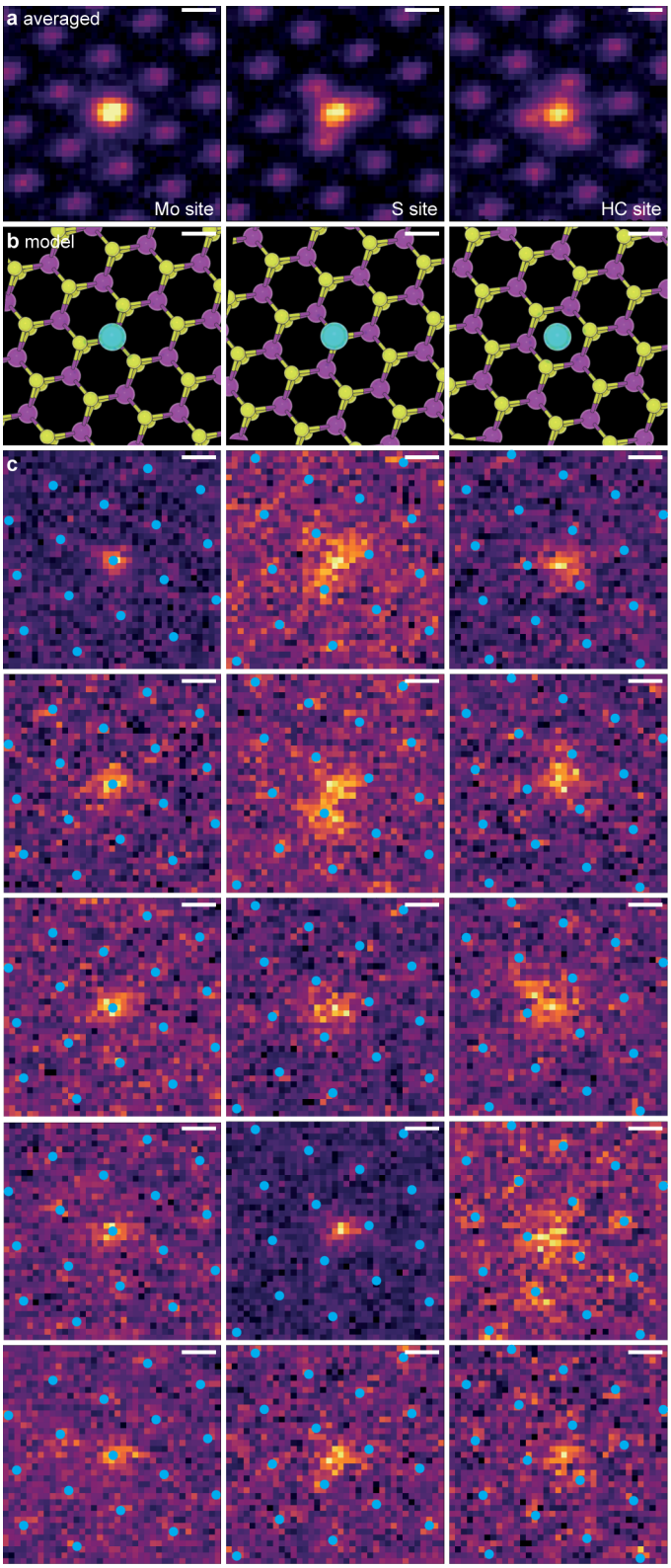

Figure S2 Identification of the position of Pt adatoms on a MoS_2 lattice inside a liquid cell. *(a) HAADF STEM images of identified Pt adatoms at Mo, S, and centre (HC) sites. Contrast has been improved by averaging over many similar sites. (b) Schematic atomic models showing the assumed atomic positions of the Pt atoms relative to the MoS_2 lattice. Mo atoms are shown in purple, and S in yellow, with Pt in light blue. (c) additional examples of raw HAADF STEM images showing Pt adatoms located at the different sites (similar to figure 2c in the main text). Blue dots indicate Mo site locations identified by template matching. Scale bars are 200 pm.*

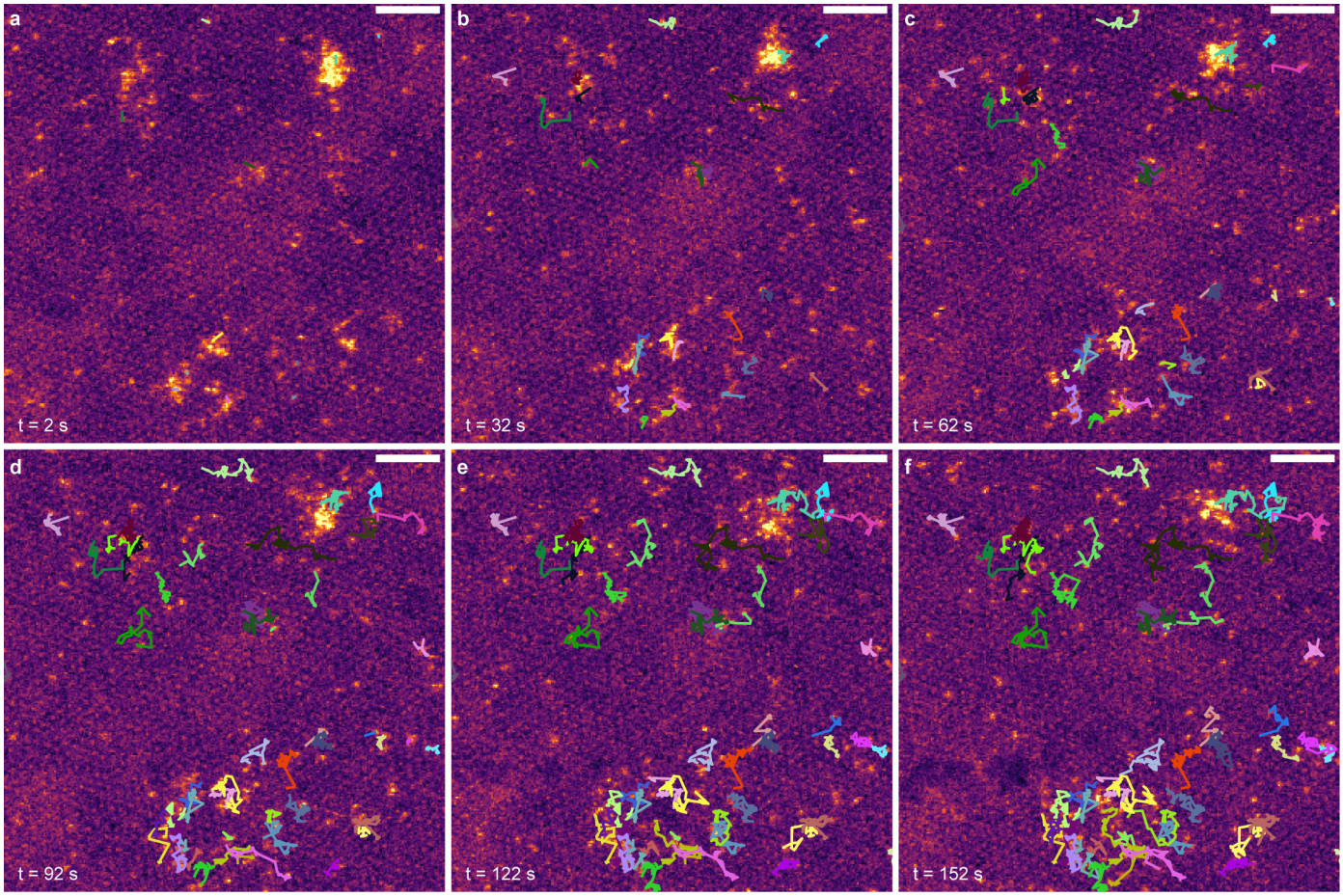

Figure S3 Example Pt adatom trajectories. *Wider view of figure 4b main text, where HAADF STEM images are overlaid with evolving particle tracks that are coloured according to the individual atom to which the trajectory corresponds (rather than colour changing with time as in figure 4b). Scale bars are 2 nm.*

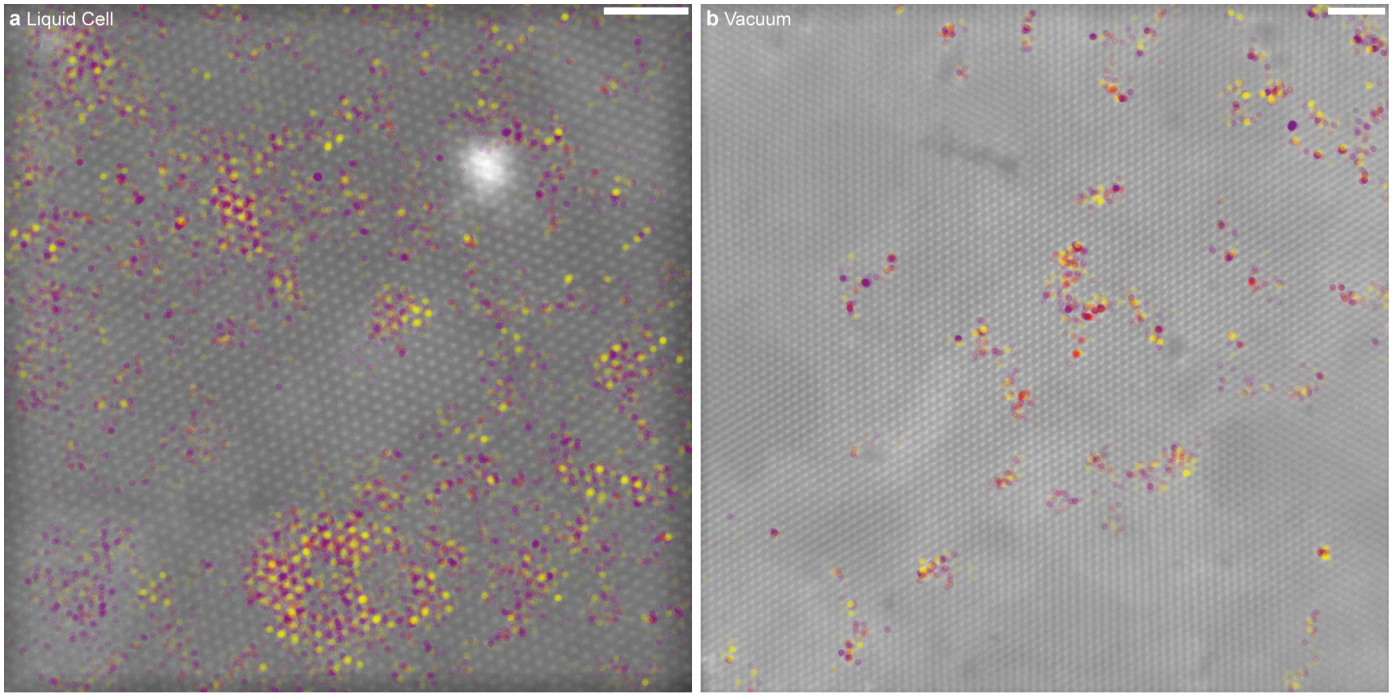

Figure S4 Overlay showing all locations of identified adatoms. *All identified adatom sites for (a) liquid cell (supplementary video 4) and (b) in vacuum (supplementary video 5), plotted on the time integrated video (after drift correction). The colour of the dot indicates the nature of the underlying lattice site: purple for Mo, yellow for S, red for HC. Dots are transparent so a brighter dot means longer total occupancy of that site. Scale bars are 2 nm.*

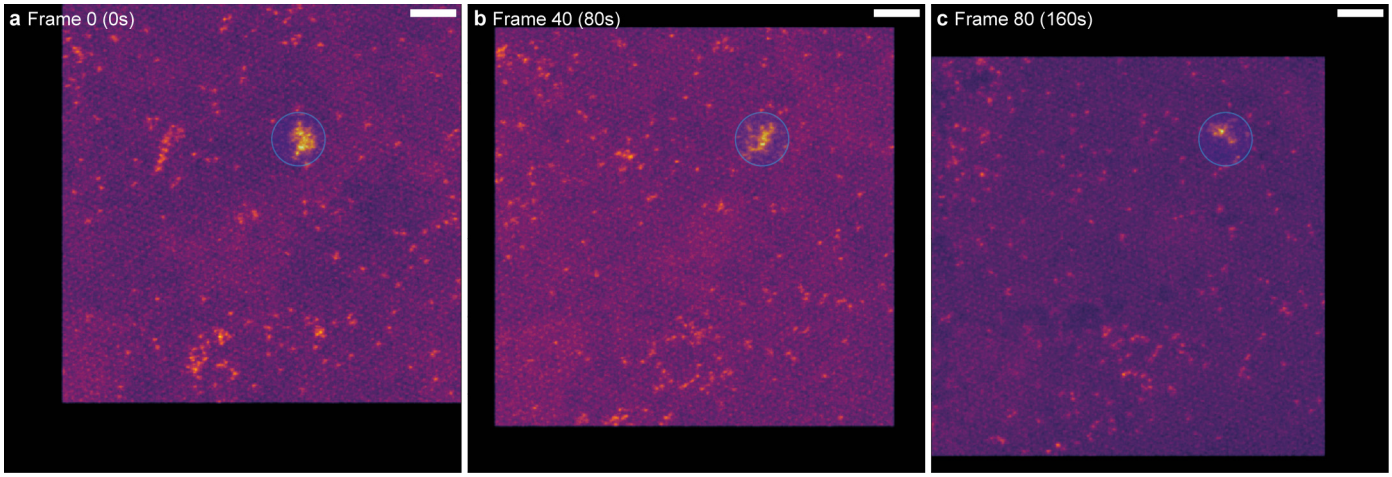

Figure S5 Excluding regions of high Pt concentration from data analysis. *Three frames from supplementary video 4 at times of 0s, 80s, and 160s respectively. Images are drift corrected to aid understanding. Blue circle indicates an area of high Pt dopant concentration where identified atoms were not used to generate position histogram (figure 3a) or linked during trajectory search. Scale bars are 2 nm.*

4. Statistical Analysis of Atomic Motion

Here we describe the method used for estimation of quantitative data on dynamic motion and diffusion from the atomic resolution atom tracking. For a typical Brownian diffusion process, the mean square displacement (MSD) of an ensemble of particles is linear with time, and is given by the Einstein–Schlomuski relationship:

$$\langle \vec{r}^2(\Delta t)\rangle = \left\langle \left(\vec{r_i}(t+\Delta t) - \vec{r}_i(t)\right)^2 \right\rangle = D\Delta t \quad (E1)$$

where $\vec{r}_i(t)$ is the position of particle i at time t, and D is a diffusion constant. For this to hold true, the particles are required to be independent, and the particle displacements must be symmetric (in time and space) and statistically independent. Brownian motion in two dimensions has been previously observed for nm-scale clusters in liquid cells[17,73,74]. When any of these assumptions break down there is a non-linear relationship between the MSD and time, usually characterized as a power law:

$$\langle \vec{r}^2(\Delta t)\rangle = D_\propto \Delta t^\propto \quad (E2)$$

where $D_\propto$ and $\propto$ are termed the anomalous diffusion coefficient and exponent respectively. Anomalous diffusion can be characterized as subdiffusive motion (when $\propto < 1$) and superdiffusive motion[75] (when $\propto > 1$). As shown in figure 4 in the main text, we clearly observed subdiffusive motion for Pt adatoms on MoS_2, in both vacuum and liquid environments.

As well as the non-linearity of the MSD, we can also consider the ergodicity of the process. A diffusion process is ergodic if the ensemble diffusion properties can be deduced from a long observation of a single trajectory. This requires both that individual particle trajectories are statistically indistinguishable, and that the process increments are stationary, i.e. do not change with time. Diffusion processes are typically analysed by calculating the time-first averaged mean squared displacement (TAMSD). For discrete data, this takes the form:

$$\langle \vec{r}^2(\Delta t)\rangle = \left\langle \left(\vec{r}(t+\Delta t) - \vec{r}(t)\right)^2 \right\rangle = \frac{1}{N_p}\sum_{i=1}^{N_p} \frac{1}{T_i - \Delta t} \sum_{t=t_0}^{T_i-\Delta t} \left(\vec{r_i}(t+\Delta t) - \vec{r_i}(t)\right)^2 \quad (E3)$$

where the individual deviations for each particle trajectory (from time t_0 to T_i) are first averaged across all time gaps), before being averaged over the ensemble of N_p particles. This TAMSD is the quantity which is plotted in figure 4d in the main text. The results after the first summation, $\vec{r}_i^{\,2}(\Delta t)$ are a mean squared displacement for each individual trajectory and are termed the individual mean squared displacement (IMSD). Before the second summation, the IMSD were weighted according to equation B4 in reference[76] to account for the fact that measurements on a single trajectory are not statistically independent (not shown in equation E3).

We can also calculate the ensemble-averaged first mean square displacement (EAMSD):

$$\overline{\vec{r}^2(\Delta t)} = \overline{\left(\vec{r}(t+\Delta t) - \vec{r}(t)\right)^2} = \frac{1}{T_i - \Delta t}\sum_{t=t_0}^{T_i-\Delta t} \frac{1}{N_p}\sum_{i=1}^{N_p} \left(\vec{r_i}(t+\Delta t) - \vec{r_i}(t)\right)^2 \quad (E4)$$

where deviations are first averaged over all particles in the ensemble before being averaged across all times. The quantities after the first summation, $\vec{r}^2(t, \Delta t)$, are known as the moments of stationarity. For an ergodic process, the TAMSD and EAMSD are equivalent.

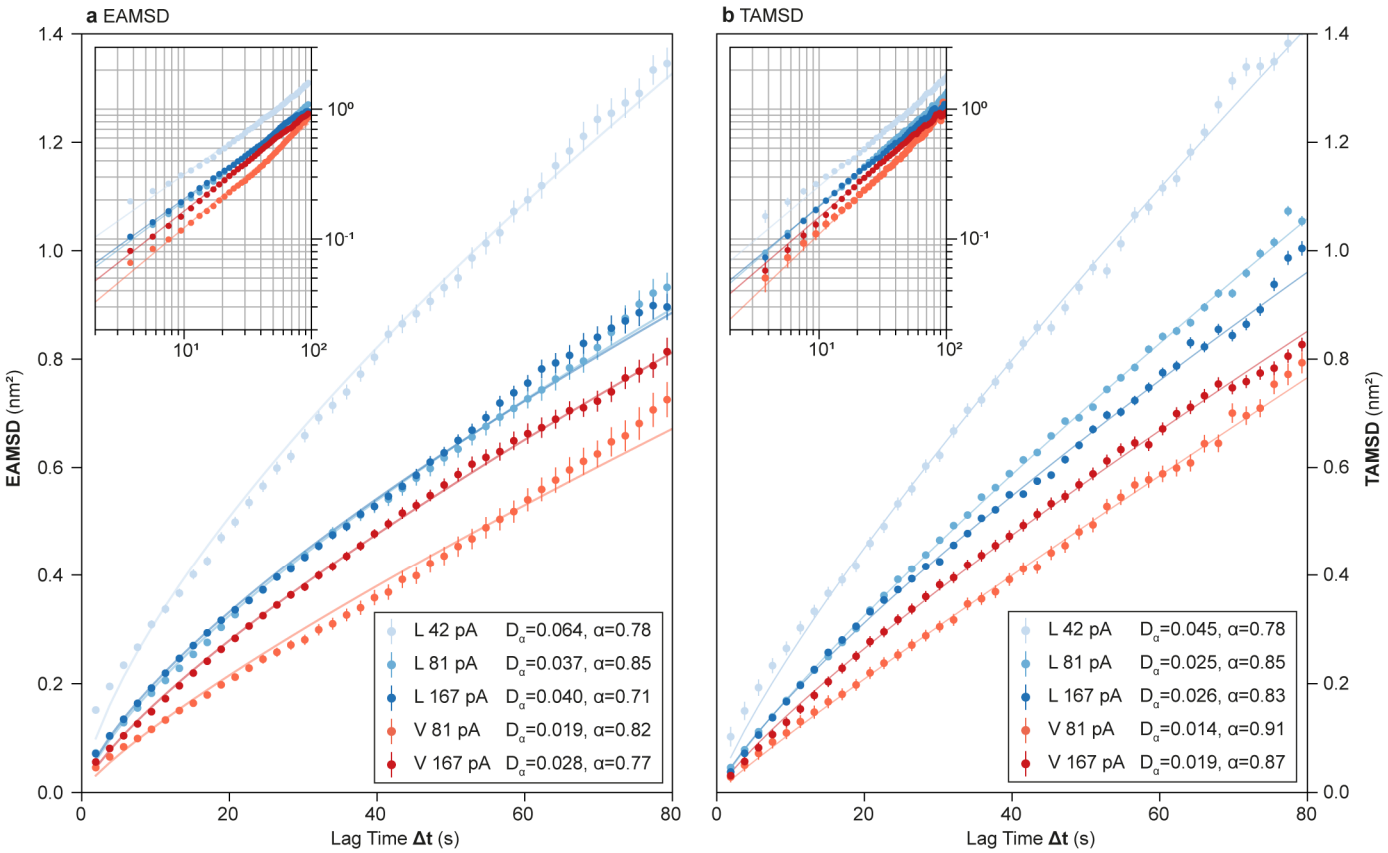

Figure S6 Comparison of time first averaged mean square displacements (TAMSD) and ensemble first averaged mean square displacements (EAMSD)*. Fit coefficients corresponding to a power law fitting function are shown in the inset. Bars represent the calculated standard error.*

The TAMSD and EAMSD for the particles in supplementary videos 4-8, are shown in figure S6. The values of the coefficient and exponent after fitting to a power law (as in equation S2) are given in the legend with the graphs plot on a logarithmic scale in the inset. Importantly the relative difference between the liquid and vacuum data sets is consistent and much larger than the differences for the TAMSD and EAMSD measurements of the same data. There are small differences between the TAMSD and EAMSD for all data sets, with the EAMSDs indicating more subdiffusive motion.

To investigate the reasons for the observed differences in TAMSD and EAMSD it is informative to look at the distribution of individual mean square displacements (IMSD) and the moments of stationarity. IMSDs corresponding to individual Pt adatom trajectories from supplementary videos 4 and 5 are shown in figure S7a-b The IMSDs were fit to a power law function as in equation S2 and the distribution of the fit parameters D_α and α are also shown, along with the plotted trajectories of adatoms with relatively high (green) and low (red) fit parameters. The distribution of the individual particle trajectory exponents α is similar in both cases, peaked around $\alpha \approx 0.9$, with the exception of an increased population of highly subdiffusive particles ($\alpha \approx 0.4$) in vacuum (suggested as being associated with sulphur vacancies – see main text discussion). This extra 'subdiffusive population' is the cause of the difference in fit exponent for the TAMSD, rather than any difference for the whole population.

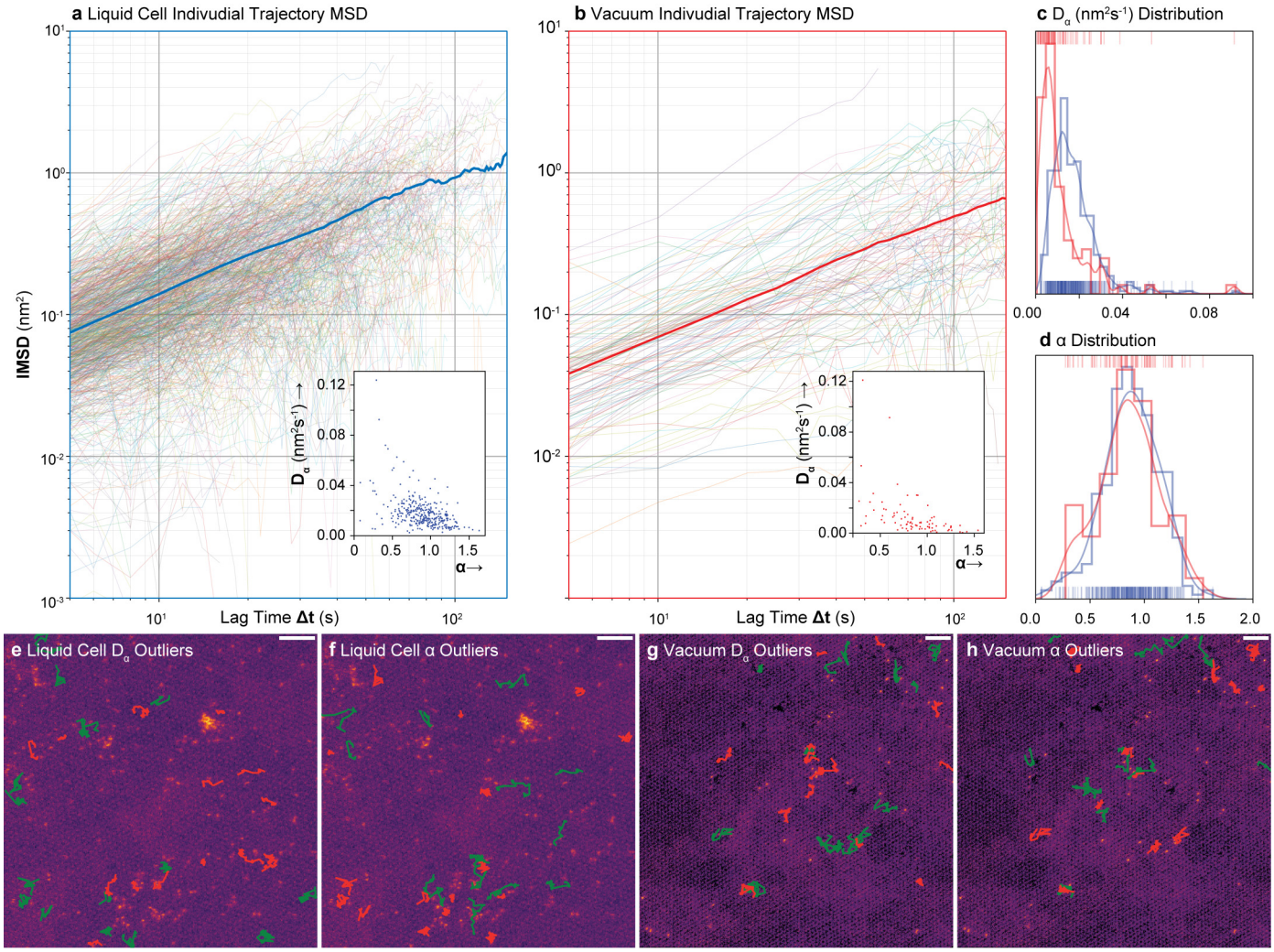

Figure S7 Individual Particle Trajectory (Time-averaged) MSD plots for liquid cell data (video S4) and vacuum data (video S5). *(a, b) Plot of MSD vs time for each trajectory in the Liquid Cell video S4 and Vacuum Particle tracking video S5 sequences. The bold line shows the (ensemble averaged) TAMSD. The insets show the distribution of power law fit parameters for each trajectory. (c, d) Histograms of the two fit parameters, the coefficient D_α and the exponent α. (e, g) show the trajectories in both videos which have large (coloured green) and small (coloured red) coefficients D_α, and (f, h) show trajectories with outlying values of the exponent α. Note that many of the individual tracks do not span the full time of the video – during imaging adatoms can appear spontaneously due to deposition onto the MoS_2 surface from the liquid phase, and vice versa a loss of Pt adatoms into the liquid. Scale bars are 2 nm.*

Extended data figure 7 shows further analysis to rule out potential sources of error for the analysis presented (e.g. artefacts due to atoms passing close to each other). Extended data figure 7a demonstrates that the number of atoms being measured and the areal densities are roughly constant as a function of times for all the video series analysed in this work. Extended data figure 7c provides the analysis of TAMSD displacements where we consider only isolated particles, with nearest neighbour distances greater than 1 nm, and compare these to the full data set. Both data sets show similar behaviour, which gives us confidence that atom interactions between individual Pt atoms has negligible impact on the analysis we present.

By comparing the Pt adatom trajectories to the inferred positions of the Mo lattice sites, we can calculate the relative probabilities of the various atomic site transitions between frames. The preferred positions of Pt adatoms relative to the underlying lattice is shown in figure 3 in the main text, but we can also investigate how the original lattice site affects the directionality and distance of the Pt motion. Extended data figure 8a shows the chance of a Pt adatom identified as occupying one of the three sites (Mo, S, HC) remaining stuck on the same specific site in the next frame, as calculated for each recorded image sequence. This ‘stuck’ probability is significantly higher in vacuum for all lattice sites. Extended data figure 8a also shows that in both liquid and vacuum environments, Pt atoms are more likely to ‘stick’ for prolonged periods at sulphur sites, a reflection of the fact that a proportion of the Pt are likely occupying sulphur vacancies rather than adsorbed on top of the pristine lattice. Extended data figure 8b shows the relative chance of an adatom staying on the site for n frames as a function of n. Similar to Extended data figure 8a, this data shows that Pt is less likely to ‘stick’ at a single site for prolonged periods in the liquid compared to vacuum, and that for both liquid and vacuum environments S sites are the most ‘sticky’ while HC sites are the least ‘sticky’. Extended data figure 8c illustrates the relative chances of Pt adatoms jumping to adjacent lattice sites in both liquid and vacuum environments.

5. Dose dependence of atomic motion

Figure 3 in the main text presents spatially resolved histograms as a function of electron probe current (42 – 167 pA) with fixed pixel dwell time, scan size and imaging area. This equates to a range of electron flux from 0.7 – 2.8 x 10^6 e nm^{-2} s^{-1}. The preferred lattice sites for the adatoms we observe in a liquid environment show the same qualitative behaviours for all electron probe currents. Similarly, we do not observe any difference in the relative Pt adatom distribution on the support in vacuum as a function of electron flux (either for the *ex situ* sample or after dehydration of the liquid). This dose range represents three common imaging conditions and covers the full range of electron fluxes that is practical using our experimental setup: higher flux and the beam degradation of the MoS_2 support layer made the videos increasingly short and prone to specimen drift while lower flux reduced the signal to noise ratio (SNR) such that we were no longer able to distinguish the Mo lattice sites.

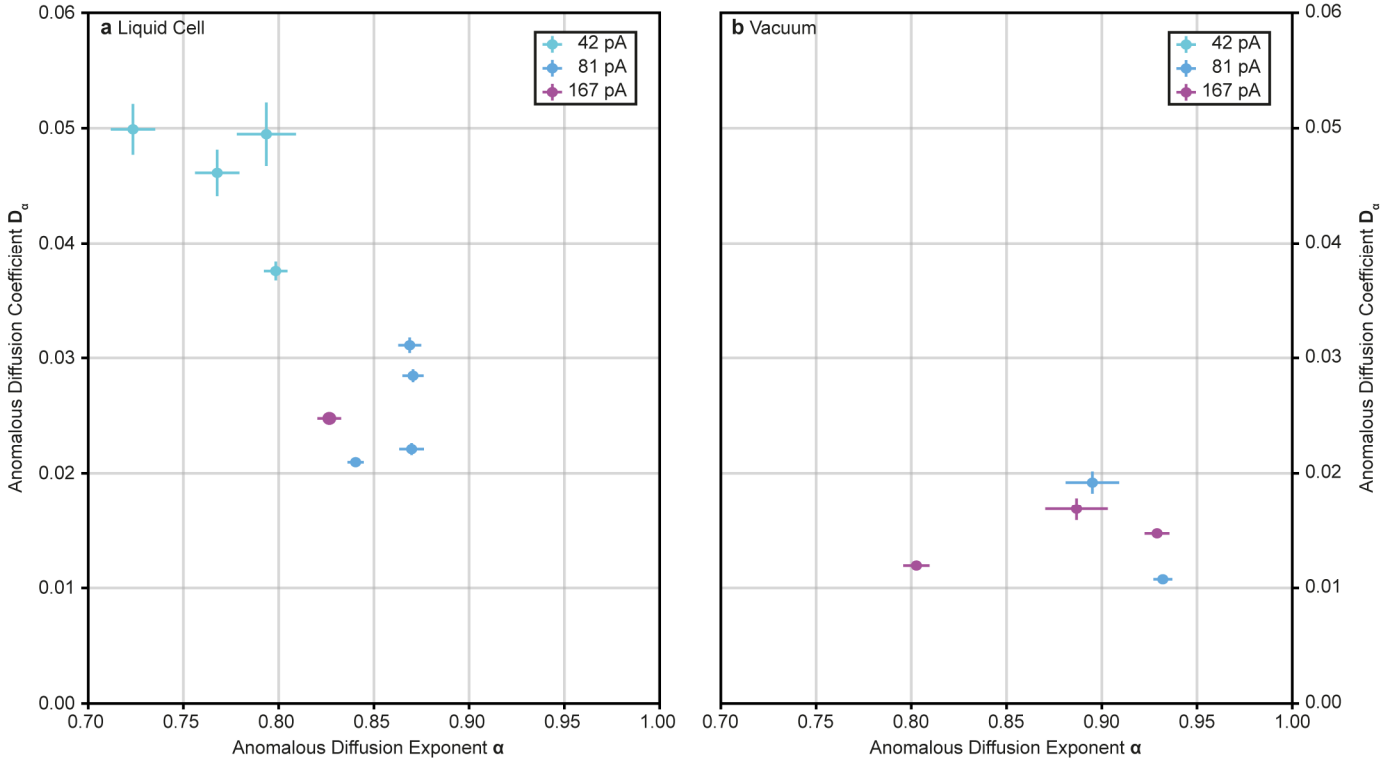

Figure S8 Comparison of MSD fit power law fit parameters with varying electron beam current. *(a) and (b) show the TAMSD fit parameters for the various recorded videos in liquid and vacuum respectively. They are coloured according to the electron beam current. (c) calculated mean square displacement for a lag time ΔT = 10s as a function of beam current. Bars represent standard error.*

We also studied the effect of electron flux on the adatom dynamic motion (Figure S8). Beam currents of 81 – 167 pA are indistinguishable in both liquid and vacuum environments, yielding anomalous diffusion coefficients $D_{\alpha,liquid}$ = 0.025 ± 0.002 and $D_{\alpha,vacuum}$ = 0.015 ± 0.002, and anomalous diffusion exponents of α_{liquid} = 0.86 ± 0.01 and α_{vacuum} = 0.88 ± 0.02. However, when the lowest current is used we measure a significantly increased diffusivity (higher $D_{\alpha,liquid}$) and increased subdiffusivity, (lower α_{liquid}) in the liquid cells. This is surprising as for an electron beam driven diffusion process we would expect a lower electron dose to generate the opposite: lower diffusivity and a more Brownian-type diffusion behaviour α=1. We hypothesise that this opposite behaviour may be because at higher electron flux the electron beam creates many free radicals and defect sites that interact with the adatoms slowing atomic motion, while when the flux is lowered the prevalence of these is lower. In principle, it should be possible to eliminate the effect of the electron beam entirely by comparing images after longer delays with the electron beam blanked. However, in this

case it was impossible to link atoms between non-consecutive frames due to their large motion and indistinguishable nature combined with the uncertainty caused by spatial drift. Further work is required to fully understand the potential for electron flux to control beam induced motion of adatoms in liquids.

6. Density functional theory simulations

We complement our experimental observations with density functional theory calculations. Ideally such calculations would consider both liquid and vacuum environments, but full consideration of a complex liquid environment is a huge computational effort. Nonetheless, calculations that neglect the presence of the liquid can provide useful additional information on the binding and diffusion of Pt at pristine and defective MoS_2, the role of oxygen substitution into S vacancies, and the possible effect of charge states.

Role of O substitution into S Vacancy

Experimentally we find that for vacuum measurements the Pt atoms show a clear preference to sit above the S sites in the MoS_2 lattice, Figure 3e in main text. This is despite theoretical calculations indicating that the preferred lattice position for the Pt is above the Mo site in pristine MoS_2 [24,30], with metastable states above S and HC sites. This result is consistent with previous *ex situ* data[30] and has been attributed to the presence of S vacancies which present more energetically favourable positions.

To understand this in more detail we performed a series of DFT calculations of Pt binding to pristine and defective MOS_2. Adsorption energies under various conditions are compared, which we define as:

$$\Delta E_{ads} = E_{MoS_2} + E_{Pt} - E_{Pt@MoS_2} \quad (E5)$$

where E_{MoS_2}, E_{Pt} and $E_{Pt@MoS_2}$ are the total energy of the MoS_2 slab (with or without a vacancy), the total energy of a Pt atom in the gas phase, and the total energy of the adsorption system with the Pt adatom adsorbed on the MoS_2 slab (again with or without a vacancy). From these calculations we find that the Pt binding energy on pristine MoS_2 at Mo sites is 3.5 eV and 3.1 eV at S sites. In contrast, the Pt binding energy on a S vacancy is almost twice as large at 6.1 eV. Thus, we can expect that a Pt atom will preferably bind to S vacancies.

Also, Pt diffusion from a S vacancy to other S sites is a highly endothermic process (extended data figure 9a) with barrier of 3.1 eV, as computed from nudged elastic band (NEB) calculations[77]. A transition state in the Pt diffusion path is identified from the NEB energy profile and vibrational mode analysis ω_i = 30i cm^{-1} (extended data figure 9a). The transition state is located at a highly asymmetric point near the S top site. Once a Pt adatom is trapped at a S vacancy, the adatom is not easily able to thermally diffuse into other sites. This binding energy is also above the energy which can theoretically be provided by a 200 keV electron (2.69 eV calculated according to ref. [32]) which supports the observation that such sites act as prolonged adsorption sites, especially in the vacuum environment.

In the liquid environment, we observe similar occupancies for Mo and S sites while in vacuum the S sites are the preferred adsorption site (figure 3 in main text). The electron beam energy (200 keV) is above the threshold required to create S vacancies in MoS_2, but we propose that the difference in behaviour is because in the presence of aqueous liquid these vacancies are able to substitute with oxygen from the liquid (as has previously been observed with adsorbed oxygen containing contaminants[30]).

To investigate the potential role of O substitution on a S vacancy, we calculated the Pt binding energy to MoS_2 where an S vacancy is occupied by an oxygen atom. From our DFT calculations, we observe that an O atom (9.12 eV) binds more strongly than Pt (6.08 eV) to a S vacancy site. Thus, it is plausible to assume that the O atom preferentially occupies the S vacancy site over Pt atoms in an aqueous environment. Further calculations show that Pt adatoms do not favour to sit above the substituted oxygen site (Pt@O) but can lower the energy of the system by moving to a pristine S site (Pt@S) (extended data figure 9b). A diffusion from the substituted oxygen site to S site is an almost barrierless (~0.01 eV) process and Pt adsorption on O site can be considered as a metastable state.

Thus, we can conclude that in aqueous conditions (1) Pt adatoms will not be trapped in S vacancy sites because these will be preferentially occupied by oxygen and (2) Pt adatoms will preferentially diffuse along pristine Mo or S sites while avoiding O sites. This may be a contributing factor to the increased subdiffusivity we observe experimentally in liquid, as the presence of unfavourable oxygen substituted S vacancies could reduce the dimensionality of available jumps leading to more subdiffusive motion.

Effect of charge state of Pt adatoms

We have then used DFT calculations to investigate the effect of charged Pt (Pt^{+1}/Pt^{-1}) on the Pt diffusion for pristine MoS_2. Charge population analysis based on density functional theory does not necessarily yield formal charges (+1, -1, etc.) with the numbers often being low. We calculated the charge state of a Pt adatom in a neutral, reduced (excess electron) and oxidised (too few electron) environment, with the results summarised in extended data table 2 using the Bader charge analysis approach[78]. These calculations were performed by adding or removing an electron to the periodic unit cell, with the Makov-Payne correction[79] applied. We note a general trend in that the Pt adatoms that sit at Mo-sites have a tendency to be more oxidised than those on S-sites, which is consistent with previous work[30].

To gain insights into the experimentally observed diffusion kinetics, we further compared the energy difference between Pt on a Mo-site (Pt@Mo) and Pt on a S site (Pt@S) for the three environments (neutral, reduced, and oxidised) as shown in extended data figure 9c-d. The comparison of relative energy levels provides insight as to whether the redox state of Pt will play an important role in determining a dominant diffusion pathway, i.e., Mo top → Mo top. For all three environments, the Pt adatom prefers to sit above the Mo top site, and the Pt binding energy differences between the Mo top and S top sites are similar in all cases, 0.41-0.45 eV (extended data figure 9c).

The transition pathway shows that the diffusion barrier of charged Pt (+1/-1) is reduced to 0.35 eV (oxidised Pt) and 0.36 eV (reduced Pt) compared to 0.57 eV (neutral Pt). The two local basins of the oxidised Pt energy pathway come from large structural distortions of S atoms due to the positively charged Pt adatom nearby.

References

50 Gorbachev, R. V. *et al.* Hunting for Monolayer Boron Nitride: Optical and Raman Signatures. *Small* **7**, 465-468 (2011).

51 Blake, P. *et al.* Making graphene visible. *Appl. Phys. Lett.* **91**, 063124 (2007).

52 Reina, A. *et al.* Transferring and Identification of Single- and Few-Layer Graphene on Arbitrary Substrates. *J. Phys. Chem. C* **112**, 17741-17744 (2008).

53 Frisenda, R. *et al.* Recent progress in the assembly of nanodevices and van der Waals heterostructures by deterministic placement of 2D materials. *Chem. Soc. Rev.* **47**, 53-68 (2018).

54 Dean, C. R. *et al.* Boron nitride substrates for high-quality graphene electronics. *Nat. Nanotechnol.* **5**, 722-726 (2010).

55 Meyer, J. C. *et al.* Accurate measurement of electron beam induced displacement cross sections for single-layer graphene. *Phys. Rev. Lett.* **108**, 196102 (2012).

56 Kotakoski, J., Santos-Cottin, D. & Krasheninnikov, A. V. Stability of Graphene Edges under Electron Beam: Equilibrium Energetics versus Dynamic Effects. *ACS Nano* **6**, 671-676 (2012).

57 Komsa, H.-P. *et al.* Two-Dimensional Transition Metal Dichalcogenides under Electron Irradiation: Defect Production and Doping. *Phys. Rev. Lett.* **109**, 035503 (2012).

58 Kretschmer, S., Lehnert, T., Kaiser, U. & Krasheninnikov, A. V. Formation of Defects in Two-Dimensional MoS2 in the Transmission Electron Microscope at Electron Energies below the Knock-on Threshold: The Role of Electronic Excitations. *Nano Lett.* **20**, 2865-2870 (2020).

59 Zan, R. *et al.* Control of radiation damage in MoS_2 by graphene encapsulation. *ACS Nano* **7**, 10167-10174 (2013).

60 Egerton, R. F., Li, P. & Malac, M. Radiation damage in the TEM and SEM. *Micron* **35**, 399-409 (2004).

61 Miller, B., Parzinger, E., Vernickel, A., Holleitner, A. W. & Wurstbauer, U. Photogating of mono- and few-layer MoS2. *Appl. Phys. Lett.* **106**, 122103 (2015).

62 Xu, Y. *et al.* Monolayer MoS2 with S vacancies from interlayer spacing expanded counterparts for highly efficient electrochemical hydrogen production. *J. Mater. Chem. A* **4**, 16524-16530 (2016).

63 Schneider, N. M. *et al.* Electron–Water Interactions and Implications for Liquid Cell Electron Microscopy. *J. Phys. Chem. C* **118**, 22373-22382 (2014).

64 Sutter, E. *et al.* In situ liquid-cell electron microscopy of silver–palladium galvanic replacement reactions on silver nanoparticles. *Nat. Commun.* **5**, 4946 (2014).

65 Cho, H. *et al.* The Use of Graphene and Its Derivatives for Liquid Phase Transmission Electron Microscopy of Radiation-Sensitive Specimens. *Nano Lett.* **17**, 414-420 (2016).

66 KC, S., Longo, R. C., Wallace, R. M. & Cho, K. Surface oxidation energetics and kinetics on MoS2 monolayer. *J. Appl. Phys.* **117**, 135301 (2015).

67 Nan, H. *et al.* Strong Photoluminescence Enhancement of MoS2 through Defect Engineering and Oxygen Bonding. *ACS Nano* **8**, 5738-5745 (2014).

68 Lu, H., Kummel, A. & Robertson, J. Passivating the sulfur vacancy in monolayer MoS2. *APL Mater.* **6**, 066104 (2018).

69 Pető, J. *et al.* Spontaneous doping of the basal plane of MoS2 single layers through oxygen substitution under ambient conditions. *Nat. Chem.* **10**, 1246-1251 (2018).

70 Zhang, W., Zou, G. & Choi, J.-H. Adsorption Behavior of the Hydroxyl Radical and Its Effects on Monolayer MoS2. *ACS Omega* **5**, 1982-1986 (2020).

71 Ardekani, H., Younts, R., Yu, Y., Cao, L. & Gundogdu, K. Reversible Photoluminescence Tuning by Defect Passivation via Laser Irradiation on Aged Monolayer MoS2. *ACS Appl. Mater. Interfaces* **11**, 38240-38246 (2019).

72 Sun, L. *et al.* Vacuum level dependent photoluminescence in chemical vapor deposition-grown monolayer MoS2. *Sci. Rep.* **7**, 16714 (2017).

73 Powers, A. S. *et al.* Tracking Nanoparticle Diffusion and Interaction during Self-Assembly in a Liquid Cell. *Nano Lett.* **17**, 15-20 (2017).

74 Zheng, H., Claridge, S. A., Minor, A. M., Alivisatos, A. P. & Dahmen, U. Nanocrystal diffusion in a liquid thin film observed by in situ transmission electron microscopy. *Nano Lett.* **9**, 2460-2465 (2009).

75 Zaburdaev, V., Denisov, S. & Klafter, J. Lévy walks. *Rev. Mod. Phys.* **87**, 483-530 (2015).

76 Qian, H., Sheetz, M. P. & Elson, E. L. Single particle tracking. Analysis of diffusion and flow in two-dimensional systems. *Biophys. J.* **60**, 910-921 (1991).

77 Henkelman, G., Uberuaga, B. P. & Jónsson, H. A climbing image nudged elastic band method for finding saddle points and minimum energy paths. *The Journal of Chemical Physics* **113**, 9901-9904 (2000).

78 Henkelman, G., Arnaldsson, A. & Jónsson, H. A fast and robust algorithm for Bader decomposition of charge density. *Comput. Mater. Sci.* **36**, 354-360 (2006).

79 Makov, G. & Payne, M. C. Periodic boundary conditions in ab initio calculations. *Phys. Rev. B* **51**, 4014-4022 (1995).